Structural strain and competition between charge density wave and superconductivity in La(Fe, Mn)As(O$_{0.89}$F$_{0.11}$) compounds

A. Martinelli ⊙,[1,*] P. Carretta ⊙,[2] M. Moroni,[2] and S. Sanna ⊙[3]

[1]*CNR-SPIN, Corso Perrone 24, I-16152 Genova, Italy*
[2]*Department of Physics, University of Pavia, Pavia, Italy*
[3]*Department of Physics and Astronomy "A. Righi", University of Bologna, University of Bologna, via Berti-Pichat 6-2, 40127 Bologna, Italy*

Selected members of the La(Fe, Mn)As(O$_{0.89}$F$_{0.11}$) system were analyzed using high-resolution synchrotron x-ray powder diffraction. The tetragonal to orthorhombic structural transition is progressively recovered in the optimally electron-doped LaFeAs(O$_{0.89}$F$_{0.11}$) phase by very light Mn substitution; at the same time, superconductivity is suppressed whereas magnetic ordering is restored. Distinct incommensurate satellite peaks develop within different thermal ranges and mark the occurrence of charge density waves characterized by distinct propagation wave vectors, as well as multiple incommensurate structural transitions; in particular, some of them arise in conjunction with the structural transformation process, disappearing after the completion of the dissymmetrization. The thermal evolution of satellite reflections observed at $\mathbf{Q} \sim 1.93$ Å^{-1} indicates a strong competition between the charge density waves and the superconductive state. A phase diagram of the La(Fe, Mn)As(O$_{0.89}$F$_{0.11}$) system is drawn on the basis of the structural, magnetic, and electronic properties of the analyzed samples.

I. INTRODUCTION

The class of compounds referred to as Fe-based superconductors has attracted huge interest since the discovery of a relatively high superconducting transition temperature (T_c) in electron-doped LaFeAsO [1]. In particular, the LnFeAs(O, F) compounds (Ln: lanthanide) belong to the so-called 1111-type family and their properties result from a delicate and tangled interplay between magnetism, superconductivity, and crystallochemistry [2]. Specifically, superconductivity is achieved by suppressing magnetism; this is usually obtained by electron doping, that is, by an appropriate chemical substitution of O with F, or even by hole doping. Pure LnFeAsO compounds undergo a structural transformation upon cooling at T_s, followed by a magnetic transition at T_m, where $T_m < T_s$ [3–7]. The origin of this structural transition is not yet clarified and it is generally ascribed to orbital or spin degrees of freedom [8–12].

Many different kinds of chemical substitution were investigated in order to gain a better comprehension of the physical properties of these materials. Among all, Mn substitution at the Fe site stands out, since it triggers unusual changes in these materials; in principle, Mn substitution should act as hole doping, but it is actually detrimental to superconductivity. In fact, optimally electron-doped La(Fe$_{1-x}$Mn$_x$)As(O$_{0.89}$F$_{0.11}$) samples exhibit an anomalously huge suppression of superconductivity by Mn substitution as small as $x \sim 0.002$, whereas static short-range magnetism is recovered for $x \geqslant 0.001$ [13,14]. In Nd- and Sm-based systems, superconduc-

tivity is also suppressed, but the amount of Mn substitution is more than 10 times larger [15,16]. The peculiar behavior characterizing the La-based system is probably related to the size of the La^{3+} ionic radius, which is the largest among Ln^{3+} ions, producing chemical pressure.

Powder diffraction analysis recently evidenced a dramatic suppression of the tetragonal to orthorhombic structural transition temperature in undoped La(Fe$_{1-x}$Mn$_x$)AsO samples ($x = 0.02$ and 0.04) [17,18]. More interesting, the occurrence of satellite peaks was detected in the low-temperature orthorhombic phase field, indicating the development of a static incommensurate modulated structure in this region [17]. These findings point to an additional charge degree of freedom, suggesting that charge density wave (CDW) instability can play a primary role in determining the structural, magnetic, and transport properties of Fe-based superconductors. Notably, a similar finding has been subsequently reported for the structurally homologue Ba(Ni$_{1-x}$Co$_x$)$_2$As$_2$ system, where the development of an incommensurate CDW state couples with a low-temperature structural transition [19]; previously, evidence for charge modulation at the Fe site was also detected in AFe$_2$As$_2$ (A = Rb, Cs) compounds by ^{75}As nuclear quadrupole resonance [20,21]. These studies disclose an alternative view for the phenomenology of Fe-based superconductors, indicating that CDW and superconductive (SC) states are adjacent and competing in the phase diagrams. Local structural analyses of the same samples evidenced an emerging disorder in the structure as well as a sharp increase in the Fe moment even with a very small amount of Mn substitution [22,23].

The aim of the present work is thus to investigate in depth the structural properties characterizing the

*alberto.martinelli@spin.cnr.it

La(Fe$_{1-x}$Mn$_x$)As(O$_{0.89}$F$_{0.11}$) system by means of high-resolution x-ray powder diffraction, and relate these properties with the transport and magnetic ones. In particular we will focus on the compositional range neighboring $x = 0.010$, where a transition from the SC to the magnetic (M) ground state is observed in the phase diagram [14]. Here we report two main outcomes. The first is the presence of structural distortions associated to the magnetic state induced by the Mn doping. The second outcome is that all the investigated samples display weak, not-indexed Bragg peaks with a strong sample dependent temperature evolution of their intensities, pointing to the presence of incommensurate modulated structure involving a CDW state.

The observed phenomenology indicates that the CDW state is ubiquitous in the LaFeAsO family, possibly pinned by the Mn impurities. Interestingly, one of the incommensurate peaks can be associated to the structural transition and one seems to be anticorrelated to the superconducting state. Finally a revised and updated phase diagram of La(Fe$_{1-x}$Mn$_x$)As(O$_{0.89}$F$_{0.11}$) which includes the structural, magnetic, and electronic properties, is drawn as a function of Mn.

II. EXPERIMENT

The sample preparation and characterization by means of electrical resistivity, superconducting quantum interference devices (SQUID) magnetometry, muon spin rotation (μSR), nuclear quadrupole, ^{75}As nuclear magnetic resonance, and extended x-ray absorption fine structure (EXAFS) are accurately described in Refs. [13–15,22,23]. In particular, μSR analysis evidenced that for samples with $x = 0.0020$, 0.0010, and 0.0075 a fully magnetic state with 100% of magnetic volume is gained just below the magnetic transition temperature, similarly to what observed in the La(Fe$_{1-x}$Ru$_x$)AsO system [24]. The nominal compositions selected for the structural analysis and pertaining to the La(Fe$_{1-x}$Mn$_x$)As(O$_{0.89}$F$_{0.11}$) system were $x = 0.00025$, 0.00075, 0.0010, 0.0020, 0.0025, 0.0050, and 0.0075. X-ray powder diffraction (XRPD) data ($l = 0.40002$ Å) were collected between 5 and 295 K (on warming) at the ID22 high-resolution powder diffraction beamline of the European Synchrotron Radiation Facility (ESRF) in Grenoble, France. In particular, samples with $x = 0.0100$, 0.0200, 0.0500, and 0.0750 were analyzed in the aforementioned thermal range, whereas samples with $x = 0.0025$ and 0.0075 were analyzed only at 295 K and the sample with $x = 0.0250$ only at 10 K.

The crystal structure was refined using the fullprof program [25]; refinements were carried out using a file describing the instrumental resolution function whereas the diffraction lines were modeled by a Thompson-Cox-Hastings pseudo-Voigt convoluted with axial divergence asymmetry function and the background by a linear interpolation between a set of fixed points. In the final cycle the following parameters were refined: the scale factor, the zero point of detector, the unit cell parameters, the atomic site coordinates not constrained by symmetry, the overall displacement parameter; and the anisotropic strain parameters. From the positions and shapes of the diffraction line profiles, the microstructure was investigated by using the refined anisotropic strain parameters
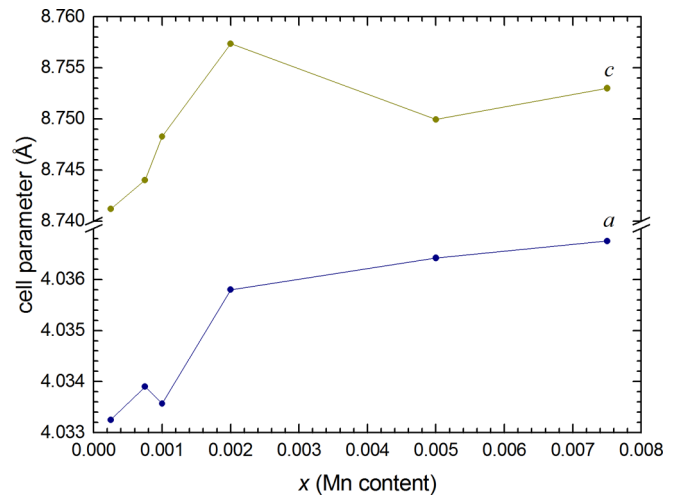

FIG. 1. Evolution of the cell parameters as a function of Mn content in La(Fe$_{1-x}$Mn$_x$)As(O$_{0.89}$F$_{0.11}$) samples at 295 K.

and analyzing the broadening of diffraction lines by means of the Williamson-Hall plot method [26]. Generally, in the case where size effects are negligible and the microstrain is isotropic, a straight line passing through all the points in the plot and through the origin has to be observed, where the slope provides the microstrain: the higher the slope the higher the microstrain. If the broadening is not isotropic, size and strain effects along particular crystallographic directions can be obtained by considering different orders of the same reflection.

III. RESULTS AND DISCUSSION

A. Structural relationships at room temperature

The Rietveld refinements carried out using XRPD data collected at 295 K reveal that all samples crystallize in the tetragonal $P4/nmm$ space group. Figure 1 shows the corresponding dependence of the cell parameters on Mn content, displaying an irregular trend centered in the compositional range ($x \sim 0.0010$) corresponding to the crossover between the superconductive and the magnetic ground state [14].

Figure 2 shows the response of the LaFeAsO structure to the chemical substitution in LaFeAs(O,F), La(Fe,Mn)AsO, and La(Fe,Mn)As(O,F); all these distortions are along {00l} and do not break the tetragonal $P4/nmm$ symmetry. In
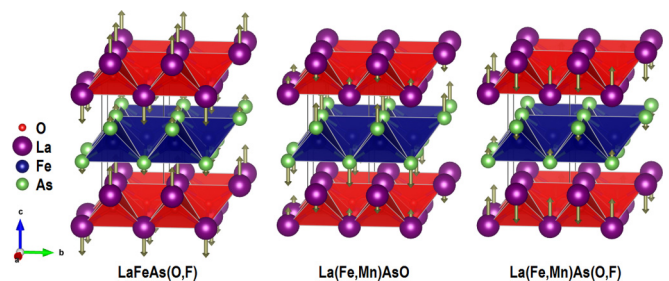

FIG. 2. Distortion patterns of the LaFeAsO crystal structure as observed for different combinations of F and Mn substitution (arrows represent atomic displacements).
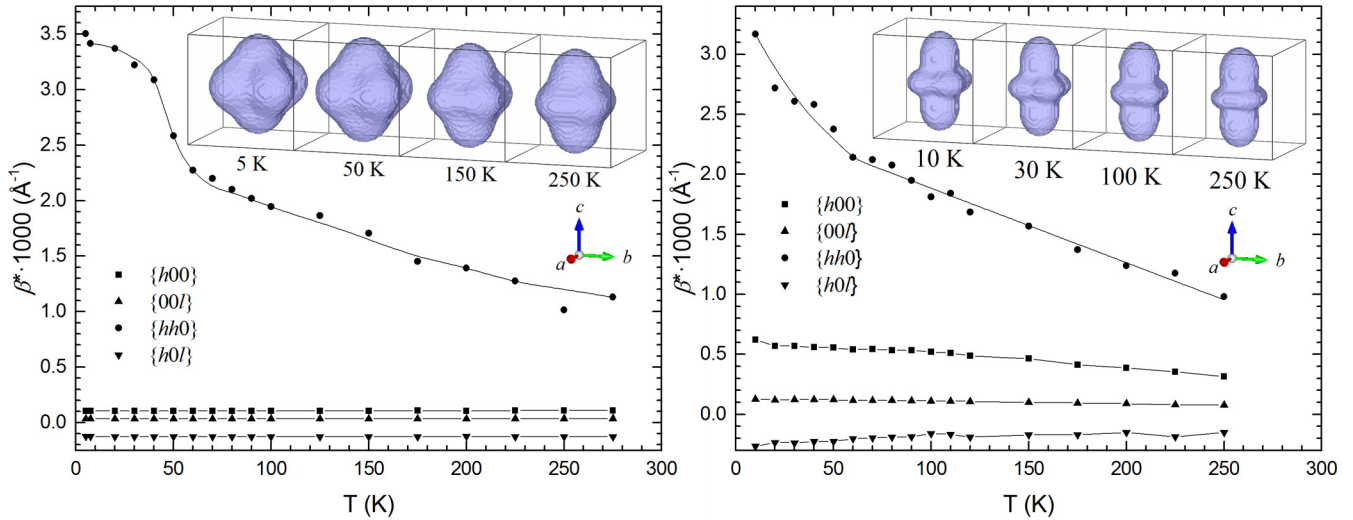
FIG. 3. Thermal evolution of the tetragonal anisotropic strain parameters obtained by Rietveld refinement for the samples $x = 0.0020$ (on the left) and 0.0010 (on the right); lines are guides to the eye; β represents the integral breadth of the diffraction line profile. The insets show the corresponding tensor surfaces calculated at selected temperatures.

LaFeAs(O,F), both tetrahedral layers are expanded along the c axis, but this effect is more pronounced for the $[LaO]^+$ layer. After Mn substitution, the crystal structure displays a notable expansion of the tetrahedral $[FeAs]^-$ layer along the c axis, slightly compressing the sandwiched $[LaO]^+$ layer. In the $La(Fe_{1-x}Mn_x)As(O_{0.89}F_{0.11})$ system, both tetrahedral layers undergo a compression along the tetragonal axis, more pronounced for the La-O layer. It is evident how layers react in opposite ways to chemical substitution in LaFeAs(O,F) and La(Fe,Mn)As(O,F) compounds. Roughly, it can be summarized that when the $[LaO]^+$ layer is electron doped by F substitution, the $[LaO]^+$ and $[FeAs]^-$ layers reciprocally attract, thus favoring the charge transfer between them; conversely, when Fe is substituted by Mn, the charge transfer is hindered on account of the $[LaO]^+$ layer compression (electrons are much more attracted by the central La^{3+} cation), disfavoring superconductivity.

B. Tetragonal to orthorhombic structural transformation

As already reported [14], Mn substitution progressively recovers the symmetry breaking that is suppressed in optimally F-doped compounds. As a rule, the structural transition in these compounds is marked by a selective peak splitting of the tetragonal hhl reflections; nonetheless, in some cases only a selective peak broadening of the same tetragonal hhl diffraction lines can be detected, depending on the amplitude of the orthorhombic distortion and/or the instrumental resolution [7,27]. In the present case, a careful line broadening analysis is required in order to recognize if and at what temperature the structural transition occurs.

Clear evidence for symmetry breaking occurrence in samples with $x = 0.0050$ and 0.0075 is provided by peak splitting of the diffraction line located at $\mathbf{Q} \sim 4.41$ Å (the 220 reflection in the tetragonal indexing; see Figs. 1 and 2 in Ref. [14]). Differently, samples with $x = 0.0010$ and 0.0020 display an asymmetric peak broadening that deserves an accurate analysis. The sample with $x = 0.0020$ is characterized by a fully magnetic ground state (static short-range mag-

netism) with a magnetic transition temperature $T_m \sim 6.5$ K, whereas superconductivity is totally suppressed [13]. Figure 3 (on the left) shows the thermal evolution of the anisotropic strain parameters along the main crystallographic directions as obtained after Rietveld refinement for the sample with $x = 0.0020$ using a tetragonal structural model in the whole inspected thermal range. The structural strain along $\{h00\}$, $\{00l\}$, and $\{h0l\}$ remains constant with temperature. Conversely, the strain along $\{hh0\}$ homogeneously increases down to ~ 60 K, then abruptly rises between 30 and 50 K and finally tends to saturate below 20 K. Notably, the strain along $\{hh0\}$ determines the selective peak broadening of the same hhl diffraction lines marking the structural transition by splitting. This behavior is typically observed also in other 1111-type compounds undergoing symmetry breaking on cooling [28–30]. The inset of Fig. 3 (on the left) displays the observed tensor isosurfaces (obtained by the refined tetragonal anisotropic strain parameters) representing the microstrain broadening characterizing the sample at selected temperatures. It is evident the development of a fourfold tensor surface in the ab plane on cooling, fully consistent with the microstrain expected for the $4/mmm \rightarrow mmm$ point group transition [31] involved in the $P4/nmm \rightarrow Cmme$ dissymmetrization. In this context, it is worth noting that no active soft mode can trigger the atomic displacements producing this in-plane microstrain observed in LnFeAsO compounds [32], demonstrating that structural degrees of freedom do not drive the structural transition. A large structural microstrain is also observed along the c axis, but remains constant in the whole inspected thermal range; as a matter of fact, this is produced by the atomic displacements described in Fig. 2 and conforms to the nonsymmetry breaking Γ_1^+ (A_{1g}) soft mode [32].

These results indicate that the crystal structure of this sample is orthorhombic at low temperature, as also confirmed by Rietveld refinements; in fact, both R_{Bragg} and R_f factors are significantly lower for the refined orthorhombic structural model ($R_{Bragg} = 4.78\%$; $R_f = 4.20\%$) in comparison with the tetragonal one ($R_{Bragg} = 5.41\%$; $R_f = 4.34\%$).
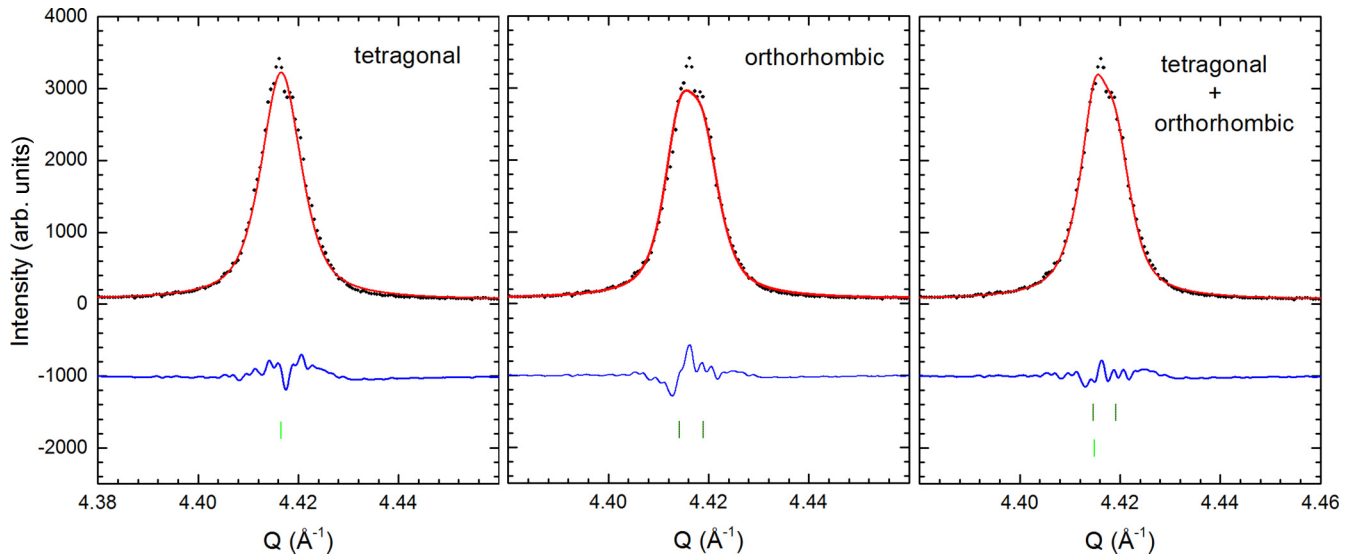
FIG. 4. Portions of full-pattern synchrotron x-ray Rietveld refinement plots for $x = 0.0010$ at 10 K showing the tetragonal 220 and orthorhombic $400 + 040$ diffraction lines fitted with different structural models.

A somehow similar behavior characterizes the sample with $x = 0.0010$, exhibiting a remarkable increase of the structural strain along $\{hh0\}$ for $T \leqslant 50$ K (Fig. 3, on the right), but no saturation at lower temperature. As for the previous sample, also the $x = 0.0010$ sample develops an in-plane fourfold tensor surface on cooling (inset of Fig. 3, on the right) consistent with the $4/mmm \rightarrow mmm$ point group transition, suggesting that even in this case a structural rearrangement is at play.

In order to determine the correct crystal structure of $La(Fe_{0.99}Mn_{0.01})As(O_{0.89}F_{0.11})$ at 10 K, three different structural models were considered: (i) a tetragonal, (ii) an orthorhombic, and (iii) a two-phase model where both polymorphs are included. The best result after convergence is achieved by applying the two-phase structural model; moreover, the refinement indicates that ~ 63 wt % is constituted of the orthorhombic phase plus ~ 37 wt % of the tetragonal polymorph (Fig. 4).

It could be argued that the presence of both polymorphs at low temperature is related to a not-homogeneous distribution of the substituting elements; this hypothesis can be ruled out after microstructural analysis. Figure 5 shows the Williamson-Hall plot obtained for the sample with $x = 0.0010$ after Rietveld refinement at 250 K, that is, in the tetragonal phase field; the straight lines in the plot provide a qualitative measurement of the structural strainlike broadening of the diffraction lines along the main crystallographic directions (the higher the slope, the higher the strainlike broadening). In the case of an irregular distribution of the substituting elements, a fluctuation of the interplanar distances is obtained for crystallites characterized by different compositions; as a result, a selective microstrainlike peak broadening occurs in the diffraction pattern. In the particular case of the tetragonal system, peak broadening should increase with the square cosine of the angle φ between the diffraction vector and the c direction. In Fig. 5 a strong microstrainlike broadening is observed along $\{00l\}$, but along $\{h0h\}$ the broadening is lower compared to the in-plane $\{h00\}$ and $\{hh0\}$ directions, indicating that compositional fluctuations are negligible and

line broadening is originated by structural microstrain caused by the atomic displacements depicted in Fig. 2.

As a matter of fact, the sample with $x = 0.0010$ is located at the crossover between the competing SC and M ground states and is electronically phase separated. In fact, previous analyses [13] revealed that a superconducting ground state characterizes this compound ($T_c = 11.5$ K); moreover, no static magnetism is present, but short-range static magnetic interactions take place at lower temperature. In particular, the magnetic fraction is ~ 55 wt % at 1.5 K, as evaluated by μSR analyses [13]; this result clearly indicates that the short-range magnetic phase develops within the orthorhombic polymorph (~ 63 wt % at 10 K).
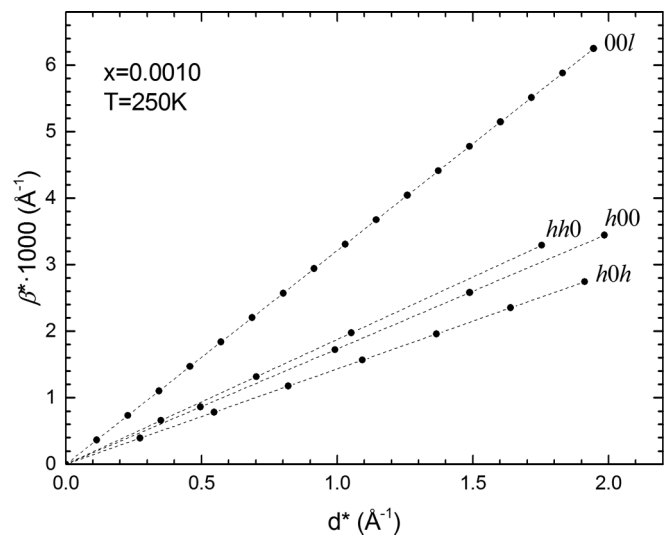

FIG. 5. Williamson-Hall plot obtained after Rietveld refinement for the sample with $x = 0.0010$ at $T = 250$ K (β represents the integral breadth of the diffraction line profile measuring the broadening produced by structural strain).
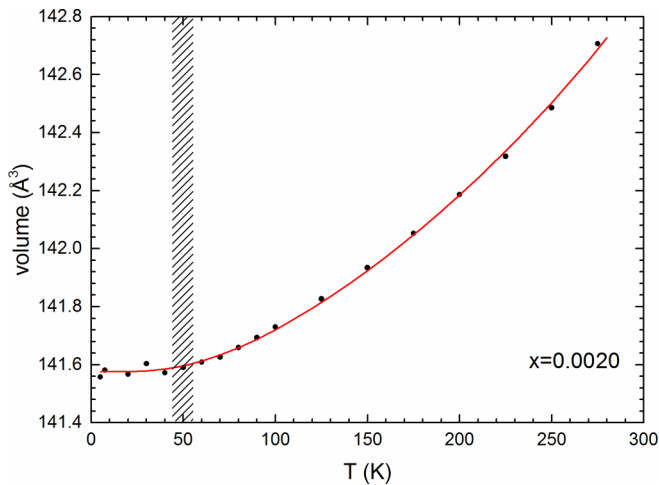
FIG. 6. Thermal expansion of the sample $x = 0.0020$, selected as representative; the hatched line represents the region where the tetragonal to orthorhombic structural transition takes place; the solid line represents the best fit to a second-order Grüneisen approximation,

The thermal expansion for the different samples was fitted using a Grüneisen second-order approximation for the zero-pressure equation of state [30,33]: The fitting was carried out assuming $K_0 = 1.03 \times 10^{11}$ Pa, which is the experimental bulk modulus value extracted from high-pressure synchrotron XRPD measurements on SmFeAs(O$_{0.93}$F$_{0.07}$) [34], and $\Theta_D = 282$ K, which is the experimental Debye temperature calculated from heat capacity data [35]. In every case the observed thermal dependence of the volume is correctly described by the Grüneisen law and no departure is observed at low temperature, in agreement with the results obtained for both La(Fe$_{1-x}$Ru$_x$)AsO and La(Fe$_{1-x}$Mn$_x$)AsO systems [18,30]; (Fig. 6) shows the result obtained for the sample $x = 0.0020$, selected as representative.

C. Charge density wave state

A closer inspection of the XRPD patterns reveals the presence of some extremely weak Bragg reflections that cannot be indexed by three-integer indices, possibly marking the occurrence of an incommensurate modulated structure involving a CDW state. In particular, these satellite reflections are observed at $Q \sim 1.93$, ~ 1.975, ~ 2.00, and ~ 2.36 Å^{-1}, but the thermal dependence of their intensities differently evolve in the different samples, pointing to distinct incommensurate periodicities taking place and vanishing at different temperatures. In this context, it is worth noting that similar multiple incommensurate structural transitions have also been reported for several other materials (see, for example, Refs. [36–41]). Notably, the satellite peak observed at $Q \sim 2.04$ Å^{-1} in the La(Fe$_{1-x}$Mn$_x$)AsO system [17] is not detected in the investigated La(Fe, Mn)As(O$_{0.89}$F$_{0.11}$) samples.

Figure 7 shows an enlarged view of the thermodiffractograms collected for the samples $x = 0.0010$ and 0.0020 in a Q region where some of these very faint satellite peaks are observed. In particular, the thermal dependence of the satellite peak located at ~ 1.975 Å^{-1} is different in these two samples. In the sample $x = 0.0010$, characterized by a fully superconductive ground state, this peak is present at high temperature, but disappears on cooling. Conversely, in the sample $x = 0.0020$, characterized by a fully magnetic ground state, it arises at low temperature in the orthorhombic phase field. In the samples with $x = 0.0050$ and $0.007\,50$ it is observed in the whole inspected thermal range (not shown). The presence of this incommensurate peak at $Q \sim 1.975$ Å^{-1} in all the samples and its disappearance for $x = 0.0010$ when cooling towards the SC state suggests a strong competition between this particular CDW and superconductivity.

Another satellite peak located at $Q \sim 2.36$ Å^{-1} appears systematically in all the samples and can likely be linked to the symmetry breaking process. In the sample $x = 0.0010$ (Fig. 8, on the left) it is only observed at 10 K, that is, in the region of the phase diagram where the superconductive tetragonal phase coexists with magnetic short-range ordered orthorhom-
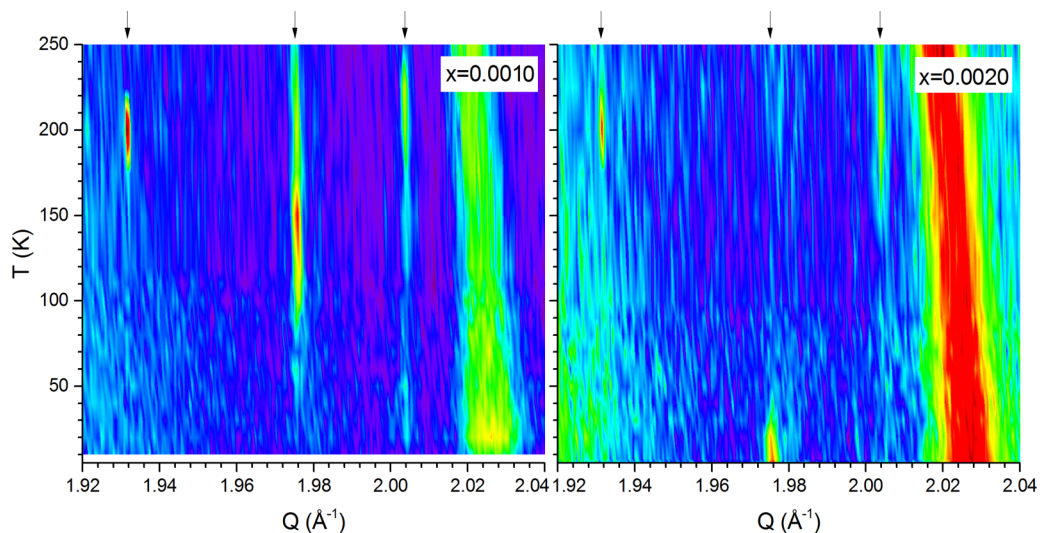

FIG. 7. Enlarged view of the thermodiffractograms for the samples with $x = 0.0010$ and 0.0020 showing the thermal dependence of the intensity of the satellite peaks located at $Q \sim 1.93$, ~ 1.975, and ~ 2.00 Å^{-1} (arrows).
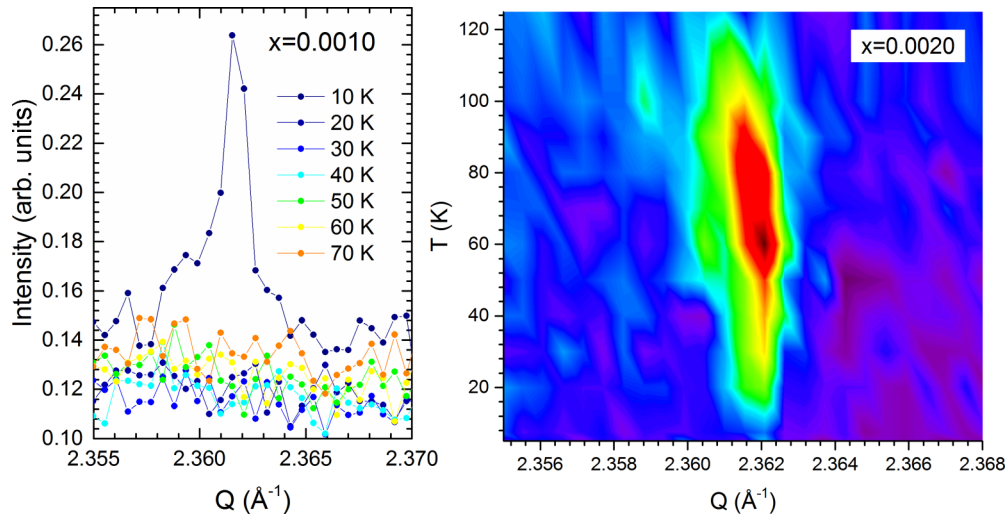
FIG. 8. Thermal evolution of the satellite peak at $\mathbf{Q} \sim 2.36 \, \text{Å}^{-1}$ in samples with $x = 0.0010$ (on the left) and $x = 0.0020$ (on the right).

bic polymorph and the anisotropic strain is maximum (Fig. 3, right panel). Conversely, in the sample $x = 0.0020$ this same satellite reflection arises below ~ 120 K, gains its maximum intensity just above the symmetry breaking (~ 60 K as shown in Fig. 3 left panel), and then rapidly decreases by further cooling until its complete suppression around ~ 10 K.

Figure 9 shows that in the sample $x = 0.0050$ this satellite peak at $\mathbf{Q} \sim 2.36 \, \text{Å}^{-1}$ is observed only in the thermal range where the tetragonal to orthorhombic transformation takes place. In the sample $x = 0.0075$ this satellite peak is shifted at a slightly lower $\mathbf{Q}$ and appears in a wider thermal range; also in this case, the satellite reflection is observed in the thermal range where symmetry breaking is observed.
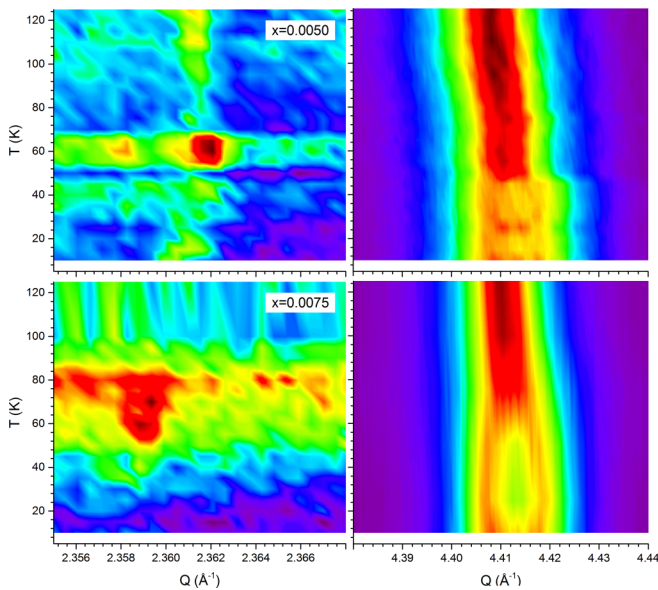
Summarizing, it can be observed that superconductivity is suppressed with the onset of the satellite peak at $\mathbf{Q} \sim 1.93 \, \text{Å}^{-1}$, demonstrating the strong competition between this particular CDW and the SC state. Moreover, a distinct CDW marked by an incommensurate reflection at $\mathbf{Q} \sim 2.36 \, \text{Å}^{-1}$ develops coupled with the structural transformation, thus likely playing a significant role in the symmetry breaking process.

D. Phase diagram of the $La(Fe_{1-x}Mn_x)As(O_{0.89}F_{0.11})$ system

Figure 10 shows the tentative phase diagram for the $La(Fe_{1-x}Mn_x)As(O_{0.89}F_{0.11})$ system as obtained by combining the structural data analyzed in the present work with
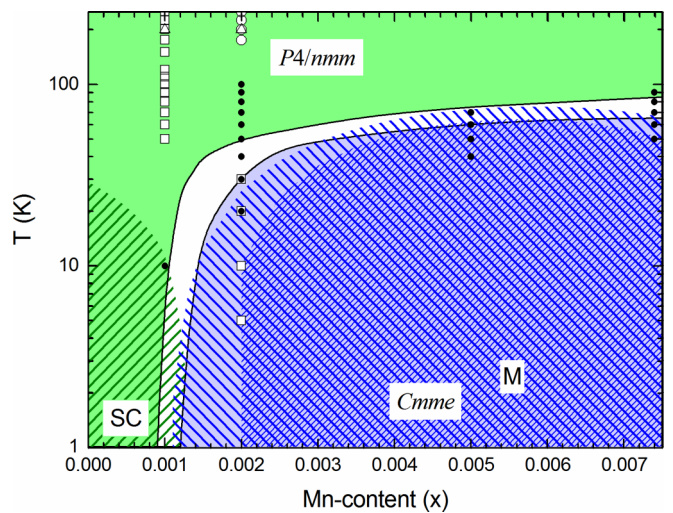

FIG. 9. Comparison between the thermal evolutions of the satellite peak at $\mathbf{Q} \sim 2.36 \, \text{Å}^{-1}$ and the tetragonal 220 diffraction line splitting into the orthorhombic 400+040 reflections in samples with $x = 0.0050$ and $x = 0.0075$.

FIG. 10. Tentative phase diagram of the $La(Fe_{1-x}Mn_x)As(O_{0.89}F_{0.11})$ system in the inspected compositional range; the magnetic phase field is drawn for both a magnetic volume fraction equal to 50% (sparse pattern) and 100% (dense pattern) (see text for details); temperatures at which incommensurate peaks are observed are also indicated ($\triangle$: CDW at $\mathbf{Q} \sim 1.93 \, \text{Å}^{-1}$; $\bigcirc$: CDW at $\mathbf{Q} \sim 1.97 \, \text{Å}^{-1}$; $\square$: CDW at $\mathbf{Q} \sim 2.00 \, \text{Å}^{-1}$; $\bullet$: CDW at $\mathbf{Q} \sim 2.36 \, \text{Å}^{-1}$).

the experimental results achieved by SQUID magnetometry, muon spin rotation (μSR), nuclear quadrupole, and ^{75}As nuclear magnetic resonance reported in Refs. [13,14]. In particular, the magnetic phase field is drawn for both a magnetic volume fraction equal to 50% (sparse pattern) and 100% (dense pattern). The onset and downset structural transition temperatures are estimated by analyzing the thermal dependence of the microstrain, the evolution in temperature of the tetragonal 220 diffraction line, and by comparing the goodness of fits obtained by applying the tetragonal, the orthorhombic, and the tetragonal + orthorhombic structural models during Rietveld refinement. Moreover, it is evident how the incommensurate satellite peaks at $\mathbf{Q} \sim 2.36\,\text{Å}^{-1}$ (● data) are observed in the thermal range where dissymmetrization occurs, whatever the composition, thus pointing to a primary role of the CDW instability in the structural transition mechanism.

A two-phase region separates the tetragonal phase field from the orthorhombic region, consistent with the first-order character of the structural transition. A crossover from the SC to M ground states occurs at the composition $x = 0.0010$; in particular, Rietveld refinement indicates that both polymorphs coexist below $\sim$50 K and that the amount of the orthorhombic structure ($\sim$63 wt %) is consistent with the magnetic phase fraction estimated by μSR analysis ($\sim$55 vol % at 1.5 K) [13]. It is not clear if the system is actually in a metastable phase, that is, if kinetics slows down the complete transformation into the orthorhombic phase, but in any case these results conceivably indicate that a short-range magnetic phase develops inside the orthorhombic structure below $\sim$5 K. With the increase of Mn content, superconductivity is entirely suppressed and magnetism becomes long-range ordered; at the same time, the structural transition completes in the whole mass on cooling and only the orthorhombic phase is found at low temperature. Notably, the downset structural transition temperature remains almost constant for $0.0050 \leqslant x \leqslant 0.0075$; conversely, the magnetic transition exhibits a maximum around $x = 0.0050$ and then decreases for higher dopings. This decoupling between the structural and magnetic transition temperatures suggests that spin degrees of freedom are not at the origin of the symmetry breaking.

IV. CONCLUSIONS

We have performed high-resolution synchrotron x-ray powder diffraction on the La(Fe, Mn)As(O$_{0.89}$F$_{0.11}$) system for $0.001 < x < 0.0075$, across the superconducting-magnetic boundary induced by Mn doping. A revised and updated phase diagram of the structural, magnetic, and electronic properties is drawn as a function of Mn content by combining SQUID magnetometry, muon spin rotation (μSR), nuclear quadrupole, and ^{75}As nuclear magnetic resonance and high-resolution synchrotron XRPD data.

The results show that the magnetic transition is associated to a structural tetragonal to orthorhombic transition and to the occurrence of an incommensurate peak at $\mathbf{Q} \sim 2.36\,\text{Å}^{-1}$, suggesting that the structural transformation is possibly driven by charge degrees of freedom, thus adding an additional ingredient in the physics of the Fe-based superconductors. Another incommensurate peak at $\mathbf{Q} \sim 1.93\,\text{Å}^{-1}$ appears to be anticorrelated to the superconducting state, demonstrating a strong competition between this particular CDW and the SC state.

Other incommensurate peaks are observed and their presence and temperature evolution are strongly sample dependent. These several incommensurate modulated structures suggest that the CDW state is ubiquitous in the LaFeAsO family, possibly pinned by the Mn impurities. The resulting scenario involves the arising of multiple incommensurate structural transitions, whose occurrence is strictly determined and ruled by thermodynamic quantities such as temperature and composition. Further studies on Mn-doped 1111 compounds in form of single crystal are needed to improve the comprehension of the interplay between structural properties, CDW, magnetism, and superconductivity in these materials.

[1] Y. Kamihara, T. Watanabe, M. Hirano, and H. Hosono, Iron-based layered superconductor La[O$_{1-x}$F$_x$]FeAs ($x = 0.05 - 0.12$) with $T_c = 26$ K, J. Am. Chem. Soc. **130**, 3296 (2008).

[2] A. Martinelli, F. Bernardini, and S. Massidda, The phase diagrams of iron-based superconductors: Theory and experiments, C. R. Phys. **17**, 5 (2016).

[3] T. Nomura, S. W. Kim, Y. Kamihara, M. Hirano, P. V. Sushko, K. Kato, M. Takata, A. L. Shluger, and H. Hosono, Crystallographic phase transition and high-T_c superconductivity in LaFeAsO:F, Supercond. Sci. Technol. **21**, 125028 (2008).

[4] J. Zhao, Q. Huang, C. de la Cruz, S. Li, J. W. Lynn, Y. Chen, M. A. Green, G. F. Chen, G. Li, Z. Li, J. L. Luo, N. L. Wang, and P. Dai, Structural and magnetic phase diagram of CeFeAsO$_{1-x}$F$_x$ and its relationship to high-temperature superconductivity, Nat. Mater. **7**, 953 (2008).

[5] J. Zhao, Q. Huang, C. de la Cruz, J. W. Lynn, M. D. Lumsden, Z. A. Ren, J. Yang, X. Shen, X. Dong, Z. Zhao, and P. Dai, Lattice and magnetic structures of PrFeAsO, PrFeAsO0.85F$_{0.15}$, and PrFeAsO$_{0.85}$, Phys. Rev. B **78**, 132504 (2008).

[6] M. Fratini, R. Caivano, A. Puri, A. Ricci, Z.-A. Ren, X-Li Dong, J. Yang, W. Lu, Z.-X. Zhao, L. Barba, G. Arrighetti, M. Polentarutti, and A. Bianconi, The effect of internal pressure on the tetragonal to monoclinic structural phase transition in ReOFeAs: The case of NdOFeAs, Supercond. Sci. Technol. **21**, 092002 (2008).

[7] A. Martinelli, A. Palenzona, C. Ferdeghini, M. Putti, and H. Emerich, Tetragonal to orthorhombic phase transition in SmFeAsO: A synchrotron powder diffraction investigation, J. Alloys Compd. **477**, L21 (2009).

[8] F. Krüger, S. Kumar, J. Zaanen, and J. van den Brink, Spin-orbital frustrations and anomalous metallic state in iron-pnictide superconductors, Phys. Rev. B **79**, 054504 (2009).

[9] W. Lv, J. Wu, and P. Phillips, Orbital ordering induces structural phase transition and the resistivity anomaly in iron pnictides, Phys. Rev. B **80**, 224506 (2009).

[10] C.-C. Chen, J. Maciejko, A. P. Sorini, B. Moritz, R. R. P. Singh, and T. P. Devereaux, Orbital order and spontaneous orthorhombicity in iron pnictides, Phys. Rev. B **82**, 100504(R) (2010).

[11] R. M. Fernandes, A. V. Chubukov, J. Knolle, I. Eremin, and J. Schmalian, Preemptive nematic order, pseudogap, and orbital order in the iron pnictides, Phys. Rev. B **85**, 024534 (2012); **85**, 109901(E) (2012).

[12] R. M. Fernandes, A. V. Chubukov, and Schmalian, What drives nematic order in iron-based superconductors? J. Nat. Phys. **10**, 97 (2014).

[13] F. Hammerath, P. Bonfà, S. Sanna, G. Prando, R. De Renzi, Y. Kobayashi, M. Sato, and P. Carretta, Poisoning effect of Mn in LaFe$_{1-x}$Mn$_x$AsO$_{0.89}$F$_{0.11}$: Unveiling a quantum critical point in the phase diagram of iron-based superconductors, Phys. Rev. B **89**, 134503 (2014).

[14] S. Sanna, P. Carretta, M. Moroni, G. Prando, P. Bonfà, G. Allodi, R. De Renzi, and A. Martinelli, Fast recovery of the pristine magnetic and structural phases in superconducting LaFeAsO$_{0.89}$F$_{0.11}$ by Mn/Fe substitution, J. Phys.: Condens. Matter **31**, 174002 (2019).

[15] M. Sato, Y. Kobayashi, S. C. Lee, H. Takahashi, E. Satomi, and Y. Miura, Studies on effects of impurity doping and NMR measurements of La 1111 and/or Nd 1111 Fe-pnictide superconductors, J. Phys. Soc. Jpn. **79**, 014710 (2010).

[16] S. J. Singh, J. Shimoyama, A. Yamamoto, H. Ogino, and K. Kishio, Effects of Mn and Ni doping on the superconductivity of SmFeAs(O,F), Phys. C (Amsterdam, Neth.) **494**, 57 (2013).

[17] A. Martinelli, P. Manfrinetti, A. Provino, A. Genovese, F. Caglieris, G. Lamura, C. Ritter, and M. Putti, Experimental Evidence for Static Charge Density Waves in Iron Oxypnictides, Phys. Rev. Lett. **118**, 055701 (2017).

[18] A. Martinelli, P. Manfrinetti, A. Provino, C. Ritter, and C. Ferdeghini, The huge effect of Mn substitution on the structural and magnetic properties of LaFeAsO: The La(Fe$_{1-x}$Mn$_x$)AsO system, J. Phys.: Condens. Matter **31**, 064001 (2019).

[19] S. Lee, G. de la Peña, S. X.-L. Sun, M. Mitrano, Y. Fang, H. Jang, J.-S. Lee, C. Eckberg, D. Campbell, J. Collini, J. Paglione, F. M. F. Groot, and P. Abbamonte, Unconventional Charge Density Wave Order in the Pnictide Superconductor Ba(Ni$_{1-x}$Co$_x$)$_2$As$_2$, Phys. Rev. Lett. **122**, 147601 (2019).

[20] E. Civardi, M. Moroni, M. Babij, Z. Bukowski, and P. Carretta, Superconductivity Emerging from an Electronic Phase Separation in the Charge Ordered Phase of RbFe$_2$As$_2$, Phys. Rev. Lett. **117**, 217001 (2016).

[21] M. Moroni, G. Prando, S. Aswartham, I. Morozov, Z. Bukowski, B. Büchner, H. J. Grafe, and P. Carretta, Charge and nematic orders in AFe$_2$As$_2$ (A = Rb, Cs) superconductors, Phys. Rev. B **99**, 235147 (2019).

[22] M. Y. Hacisalihoglu, E. Paris, L. Simonelli, B. Joseph, A. Provino, G. Lamura, A. Martinelli, P. Manfrinettig, G. Aquilanti, K. Ozturk, P. Dore, M. Putti, and N. L. Saini, The

local structure and magnetic correlations in La(Fe$_{1-x}$Mn$_x$)AsO system, J. Phys. Chem. Solids **134**, 319 (2019).

[23] M.-Y. Hacisalihoglu, L. Simonelli, C. Marini, A. Provino, A. Martinelli, P. Manfrinetti, M. Putti, and N. Saini, Mn substitution effect on the local structure of La(Fe$_{1-x}$Mn$_x$)AsO studied by temperature dependent x-ray absorption measurements, J Phys.: Condens. Matter **33**, 095803 (2021).

[24] P. Bonfà, P. Carretta, S. Sanna, G. Lamura, G. Prando, A. Martinelli, A. Palenzona, M. Tropeano, M. Putti, and R. De Renzi, Magnetic properties of spin-diluted iron pnictides from μSR and NMR in LaFe$_{1-x}$Ru$_x$AsO, Phys. Rev. B **85**, 054518 (2012).

[25] J. Rodríguez-Carvajal, Recent advances in magnetic structure determination by neutron powder diffraction, Phys. B (Amsterdam, Neth.) **192**, 55 (1993).

[26] J. I. Langford, D. Louër, E. J. Sonneveld, and J. W. Visser, Applications of total pattern fitting to a study of crystallite size and strain in zinc oxide powder, Powder Diffr. **1**, 211 (1986).

[27] A. Martinelli, A. Palenzona, M. Tropeano, M. Putti, C. Ferdeghini, G. Profeta, and E. Emerich, Retention of the Tetragonal to Orthorhombic Structural Transition in F-substituted SmFeAsO: A New Phase Diagram for SmFeAs(O$_{1-x}$F$_x$), Phys. Rev. Lett. **106**, 227001 (2011).

[28] A. Martinelli, A. Palenzona, M. Putti, and C. Ferdeghini, Microstructural evolution throughout the structural transition in 1111 oxypnictides, Phys. Rev. B **85**, 224534 (2012).

[29] A. Martinelli, A. Palenzona, M. Tropeano, C. Ferdeghini, M. R. Cimberle, and C. Ritter, Neutron powder diffraction investigation of the structural and magnetic properties of (La$_{1-y}$Y$_y$)FeAsO, Phys. Rev. B **80**, 214106 (2009).

[30] A. Martinelli, A. Palenzona, I. Pallecchi, C. Ferdeghini, M. Putti, S. Sanna, C. Curfs, and C. Ritter, Structural properties and phase diagram of the La(Fe$_{1-x}$Ru$_x$)AsO system, J. Phys.: Condens. Matter **25**, 395701 (2013).

[31] A. Leineweber, Understanding anisotropic microstrain broadening in Rietveld refinement, Z. Kristallogr. **226**, 905 (2011).

[32] A. Martinelli, Symmetry-mode and spontaneous strain analysis of the structural transition in Fe$_{1+y}$Te and REFeAsO compounds, J. Phys.: Condens. Matter. **25**, 125703 (2013).

[33] L. Vočadlo, K. S. Knight, G. D. Price, and I. G. Wood, Thermal expansion and crystal structure of FeSi between 4 and 1173 K determined by time-of-flight neutron powder diffraction, Phys. Chem. Miner. **29**, 132 (2002).

[34] A. Martinelli, M. Ferretti, A. Palenzona, and M. Merlini, The bulk modulus of SmFeAs(O$_{0.93}$F$_{0.07}$), Phys. C (Amsterdam, Neth.) **469**, 782 (2009).

[35] J. Dong, H. J. Zhang, G. Xu, Z. Li, G. Li, W. Z. Hu, D. Wu, G. F. Chen, X. Dai, J. L. Luo, Z. Fang, and N. L. Wang, Competing orders and spin-density-wave instability in La(O$_{1-x}$F$_x$)FeAs, EPL **83**, 27006 (2008).

[36] B. F. Hu, B. Cheng, R. H. Yuan, T. Dong, A. F. Fang, W. T. Guo, Z. G. Chen, P. Zheng, Y. G. Shi, and N. L. Wang, Optical study of the multiple charge-density-wave transitions in ErTe$_3$, Phys. Rev. B **84**, 155132 (2011).

[37] R. Lou, Y. Cai, Z. Liu, T. Qian, L. Zhao, Yu Li, K. Liu, Z. Han, D. Zhang, J. He, G. Chen, H. Ding, and S. Wang, Interplay between multiple charge-density waves and the relationship with superconductivity in Pd$_x$HoTe$_3$, Phys. Rev. B **93**, 115133 (2016).

[38] B. F. Hu, B. Cheng, R. H. Yuan, T. Dong, and N. L. Wang, Coexistence and competition of multiple charge-density-wave orders in rare-earth tritellurides, Phys. Rev. B **90**, 085105 (2014).

[39] R. Y. Chen, B. F. Hu, T. Dong, and N. L. Wang, Revealing multiple charge-density-wave orders in TbTe$_3$ by optical conductivity and ultrafast pump-probe experiments, Phys. Rev. B **89**, 075114 (2014).

[40] S. Shimomura, C. Hayashi, N. Hanasaki, K. Ohnuma, Y. Kobayashi, H. Nakao, M. Mizumaki, and H. Onodera, Multiple charge density wave transitions in the antiferromagnets RNiC$_2$ ($R = $ Gd, Tb), Phys. Rev. B **93**, 165108 (2016).

[41] N. S. Sangeetha, A. Thamizhavel, C. V. Tomy, S. Basu, A. M. Awasthi, P. Rajak, S. Bhattacharyya, S. Ramakrishnan, and D. Pal, Multiple charge-density-wave transitions in single-crystalline Lu$_2$Ir$_3$Si$_5$, Phys. Rev. B **91**, 205131 (2015).